Check for updates

Received: 31 May 2024 | Revised: 13 August 2024 | Accepted: 13 August 2024

DOI: 10.1002/pamm.202400200

RESEARCH ARTICLE

Isotropic growth model for generalized scaled boundary isogeometric analysis on slender structures

Florian Spahn[1] | **Florian Kolisch**[1] | **Maximilian Praster**[2] | **Elizabeth Rosado Balmayor**[2] | **Sven Klinkel**[1]

[1]Chair of Structural Analysis and Dynamics, RWTH Aachen University, Aachen, Germany

[2]Lehr- und Forschungsgebiet Experimentelle Orthopädie und Unfallchirurgie, Uniklinik RWTH Aachen, Aachen, Germany

Correspondence
Florian Spahn, Chair of Structural Analysis and Dynamics, RWTH Aachen University, Mies-van-der-Rohe-Str.1, 52074 Aachen, Germany.
Email: spahn@lbb.rwth-aachen.de

Funding information
Deutsche Forschungsgemeinschaft, Grant/Award Number: KL1345/18-1(PNO.512769030)

Abstract

Components for timber constructions are usually based on simple geometrical shapes. In the production, bifurcated or curved components of the tree crown remain unused. Recently, building botany has evolved as a new discipline of living construction design. Therefore, trees are lead in the right shape to join as a load-bearing structure interconnected with conventional parts. For the structural analysis, geometric features such as curvature or bifurcations exhibit unique static capabilities. It is crucial to transfer these geometries into the calculation model accurately. The structure can be depicted through three-dimensional scanning techniques. A fundamental model (point cloud) is created in this process. This is the base for a Non-uniform rational B-spline (NURBS) model, existing as a 2D surface within a 3D space. Using the novel generalized scaled boundary isogeometric analysis (GSBIGA)-approach, numerical disadvantages of conventional scaled boundary methods can be reduced. This method employs a scaling center line instead of a scaling center point. A growth simulation is used to describe the leading process. The present approach is based on an isotropic growth model applied to wooden growth applications. Therefore, the deformation gradient is split multiplicatively into an elastic and a growth part. The formulation for modeling volumetric growth is located on the kinematic level.

1 | INTRODUCTION

Timber is a traditional construction material; thus, a variety of criteria need to be fulfilled for its use in construction. A tree's stem should be straight, have a decent diameter, and have few branches and bifurcations concurrently. The crown of the tree, especially the crown of deciduous trees, does not fulfil these criteria. Here, the variation of different branch shapes is abundant, as each tree forms a unique geometry in the crown, influenced by the sun and damage caused by wind, snow, or animals. Traditionally, coniferous wood has been the standard for construction timber due to its straight shafts and minimal branching. However, with climate change and a shift towards a more diverse timber industry, the composition of forests is evolving. This shift creates new possibilities, with the proportion of deciduous trees in German forests projected to increase significantly [1]. The tree trunk is mainly used for further processing in a sawmill, as stated in ref. [2] for deciduous trees from German forests. The curved and bifurcated parts of the crown remain in the forest or are further processed in other ways, such as heating material, in laminated wood or nanocellulose. Utilization as load-bearing naturally shaped

This is an open access article under the terms of the Creative Commons Attribution License, which permits use, distribution and reproduction in any medium, provided the original work is properly cited.
© 2024 The Author(s). *Proceedings in Applied Mathematics* & Mechanics published by Wiley-VCH GmbH.

timber elements can save on CO_2-intensive processing. The natural shape of the timber is retained, making it easier to recycle. A demonstrator shows the feasibility of realizing a load-bearing structure using raw timber elements. Precisely recording the growth trajectories and the center lines of the timber elements is fundamental to this process. Furthermore, there are projects to grow load-bearing structures through tree manipulation and promote connections between several trees and connections with temporary support structures [3, 4]. The aim is to replace the load-bearing, technical scaffolding in the long term, but the growing structure depends on the steel support structure during its development. This process of controlled growth is known as leading. Historically speaking, the leading of trees is nothing new; before the 14th century, dance lime trees were already being led into a load-bearing structure supported by columns. In this process, the lower branches of the tree crown were artificially led into a widely stretched supporting structure to form the basis for scaffolding in the tree for dancing [5]. In order to combine these two topics, the presentation of a basic growth material and the new, naturally grown timber-related, element formulation ensues.

2 | METHOD

In this section, the applied volumetric isotropic growth material framework is first introduced. Then, the novel GSBIGA method is described.

2.1 | Growth theory

In contrast to traditional materials in civil engineering, living wood can grow to reduce the distribution of exposed stress. For the continuum mechanical description of a growing body, the theory of open systems with an internal mass source has to be applied. Thereby, the mass of a body can alter due to both a change of its volume and a change of its density. The used material model is based on Himpel et al. [6]. It is able to change its mass due to volumetric growth (and its counterpart atrophy) while preserving its density. In order to describe volumetric growth at the kinematic level, the deformation gradient $\mathbf{F}$ is multiplicatively split into a growth part, $\mathbf{F}_\mathrm{g}$, and an elastic part, $\mathbf{F}_\mathrm{e}$, as depicted in Figure 1. This split introduces an intermediate configuration (i.c.) which is usually not compatible, thus leading to elastic rest deformations and residuum stresses remaining in the system to fulfill the applied boundary conditions. Restricting the growth to isotropic volumetric growth, both parts of the deformation gradient reduce to

$$\mathbf{F} = \mathbf{F}_\mathrm{e}\,\mathbf{F}_\mathrm{g}, \quad \mathbf{F}_\mathrm{g} = \vartheta\,\mathbf{I} \quad \text{and} \quad \mathbf{F}_\mathrm{e} = \mathbf{F}\,\mathbf{F}_\mathrm{g}^{-1} = \frac{1}{\vartheta}\,\mathbf{F}, \tag{1}$$

where ϑ is the isotropic stretch ratio. To further describe the growth, the elastic Mandel stress $\hat{\mathbf{M}}$ depending on the elastic parts of the right Cauchy-Green tensor $\hat{\mathbf{C}}$ and the second Piola-Kirchhoff stress $\hat{\mathbf{S}}$ in the intermediate configuration are introduced

$$\hat{\mathbf{C}} = \mathbf{F}_\mathrm{e}{}^\mathrm{T}\,\mathbf{F}_\mathrm{e} = \frac{1}{\vartheta^2}\,\mathbf{C} \quad , \quad \hat{\mathbf{S}} = 2\,\frac{\partial \Psi_0}{\partial \hat{\mathbf{C}}} \quad \text{and} \quad \hat{\mathbf{M}} = \hat{\mathbf{C}}\,\hat{\mathbf{S}}, \tag{2}$$

where Ψ_0 is the free energy per unit volume. The evolution of the stretch ratio depends linearly on the trace of the elastic Mandel stress $\hat{\mathbf{M}}$ defined in the intermediate configuration as well as on a scaling function $k_\vartheta(\vartheta)$ which is used to prevent unlimited growth and atrophy

$$\dot{\vartheta} = k_\vartheta(\vartheta)\,\mathrm{tr}(\hat{\mathbf{M}}) \quad \text{with} \quad k_\vartheta(\vartheta) = \begin{cases} k_{\vartheta 0}^{+}\left(\frac{\vartheta^{+}-\vartheta}{\vartheta^{+}-1}\right)^{m_\vartheta^{+}} & \forall\,\mathrm{tr}(\hat{\mathbf{M}}) > 0 \quad | \,\vartheta^{+} > 1 \\ k_{\vartheta 0}^{-}\left(\frac{\vartheta-\vartheta^{-}}{1-\vartheta^{-}}\right)^{m_\vartheta^{-}} & \forall\,\mathrm{tr}(\hat{\mathbf{M}}) < 0 \quad | \,\vartheta^{-} < 1 \end{cases}. \tag{3}$$

The scalar quantities ϑ^{+} and ϑ^{-} denote the maximum and minimum value for the isotropic stretch ratio ϑ for volumetric growth ($\mathrm{tr}(\hat{\mathbf{M}}) > 0$) and atrophy ($\mathrm{tr}(\hat{\mathbf{M}}) < 0$), respectively. The other scalar quantities $k_{\vartheta 0}^{+}$, $k_{\vartheta 0}^{-}$, m_ϑ^{+} and m_ϑ^{-} are constant material parameters used to fit the material behavior. In order to describe the material model numerically, the material tangent modulus $\hat{\mathbb{C}}$ in the intermediate configuration is needed. Since the volumetric stretch ratio ϑ itself is not known but only its evolution $\dot{\vartheta}$, an implicit backward Euler method is used from the current time $(\cdot)_\mathrm{n}$ to the next time step $(\cdot)_{\mathrm{n+1}}$ with the time increment Δt with $\vartheta_{\mathrm{n+1}} = \vartheta_\mathrm{n} + \dot{\vartheta}_{\mathrm{n+1}}\,\Delta t$. For a better overview, the index n+1 is neglected in the following

16177061, 0, Downloaded from https://onlinelibrary.wiley.com/doi/10.1002/pamm.202400200 by Rwth Aachen Hochschulbibliothek, Wiley Online Library on [11/09/2024]. See the Terms and Conditions (https://onlinelibrary.wiley.com/terms-and-conditions) on Wiley Online Library for rules of use; OA articles are governed by the applicable Creative Commons License

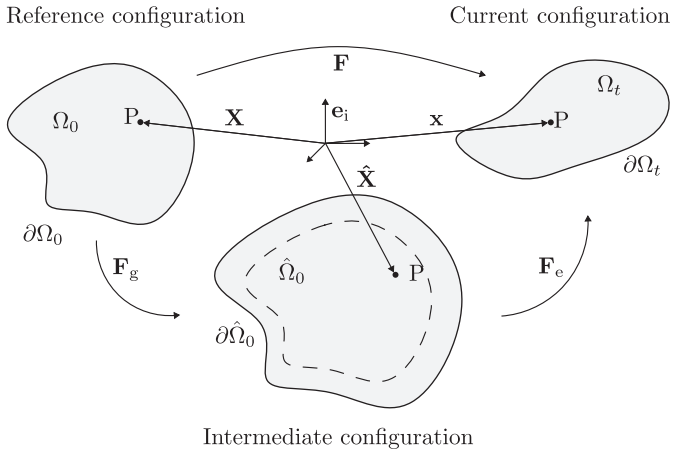


FIGURE 1 The deformation gradient $\mathbf{F}$ is split into a growth part $\mathbf{F}_g$ and an elastic part $\mathbf{F}_e$ which introduces the i.c.. The i.c. is only compatible for simple boundary conditions which justify the necessity of an elastic rest deformation. The dashed line in the i.c. shows the nongrown r.c. in the local neighborhood.

equations. Both the elastic second Piola-Kirchhoff stress $\hat{\mathbf{S}}$ and the elastic right Cauchy-Green tensor $\hat{\mathbf{C}}$ depend on the volumetric stretch ratio ϑ, thus the elastic-growth material tangent modulus in intermediate configuration in the next time step t_{n+1} is given as

$$\hat{\mathbb{C}}^{eg} = 2\,\frac{\mathrm{d}\hat{\mathbf{S}}}{\mathrm{d}\hat{\mathbf{C}}} = 2\,\frac{\partial\hat{\mathbf{S}}}{\partial\hat{\mathbf{C}}} + 2\,\frac{\partial\hat{\mathbf{S}}}{\partial\vartheta}\otimes\frac{\partial\vartheta}{\partial\hat{\mathbf{C}}} = \hat{\mathbb{C}}^{e} - \frac{2}{\vartheta}\,\overline{\partial_\vartheta\dot{\vartheta}}^{-1}\,k_\vartheta(\vartheta)\,\Delta t\,[\hat{\mathbb{C}}^{e} : \hat{\mathbf{C}}]\otimes[\hat{\mathbf{S}} + \frac{1}{2}\,\hat{\mathbf{C}} : \hat{\mathbb{C}}^{e}] \tag{4}$$

with the elastic part of the tangent modulus $\hat{\mathbb{C}}^{e}$ and the abbreviation $\overline{\partial_\vartheta\dot{\vartheta}}$ depending on the sign of the trace of the Mandel stress for growth and atrophy, respectively

$$\hat{\mathbb{C}}^{e} = 2\,\frac{\partial\hat{\mathbf{S}}}{\partial\hat{\mathbf{C}}} \quad\text{and}\quad \overline{\partial_\vartheta\dot{\vartheta}} = \begin{cases} 1 - k_\vartheta(\vartheta)\,\Delta t\left[\frac{m_\vartheta^{+}}{\vartheta-\vartheta^{+}}\,\mathrm{tr}(\hat{\mathbf{M}}) - \frac{1}{\vartheta}\left(2\cdot\mathrm{tr}(\hat{\mathbf{M}}) + \hat{\mathbf{C}} : \hat{\mathbb{C}}^{e} : \hat{\mathbf{C}}\right)\right] & \forall\,\mathrm{tr}(\hat{\mathbf{M}}) > 0 \\ 1 - k_\vartheta(\vartheta)\,\Delta t\left[\frac{m_\vartheta^{-}}{\vartheta-\vartheta^{-}}\,\mathrm{tr}(\hat{\mathbf{M}}) - \frac{1}{\vartheta}\left(2\cdot\mathrm{tr}(\hat{\mathbf{M}}) + \hat{\mathbf{C}} : \hat{\mathbb{C}}^{e} : \hat{\mathbf{C}}\right)\right] & \forall\,\mathrm{tr}(\hat{\mathbf{M}}) > 0 \end{cases}. \tag{5}$$

It is to be noted that for the elastic-growth material tangent modulus only the minor symmetry rule applies and therefore, an element capable of using asymmetric tangents in Voigt notation is necessary

$$\hat{\mathbb{C}}^{eg}_{ijkl} = \hat{\mathbb{C}}^{eg}_{ijlk} = \hat{\mathbb{C}}^{eg}_{jikl} = \hat{\mathbb{C}}^{eg}_{jilk} \quad\text{but}\quad \hat{\mathbb{C}}^{eg}_{ijkl} \neq \hat{\mathbb{C}}^{eg}_{klij} \quad\Big|\quad i,j,k,l \in \{1,2,3\}. \tag{6}$$

Since the backward Euler method leads to highly nonlinear functions of ϑ, a local Newton iteration on material level is implemented with the residuum R_ϑ which gives the stretch ratio increment $\Delta\vartheta$ to update the current Newton step $(\cdot)^k$ to the next step $(\cdot)^{k+1}$ until the absolute value of the residuum $|R_\vartheta|$ reaches a predefined limit

$$R_\vartheta = -\vartheta + \vartheta_n + \dot{\vartheta}\,\Delta t, \quad \Delta\vartheta = \overline{\partial_\vartheta\dot{\vartheta}}^{-1}\,R_\vartheta^{k} \quad\text{and}\quad \vartheta^{k+1} = \vartheta^{k} + \Delta\vartheta. \tag{7}$$

In order to use the material tangent modulus in the linearization of the weak form of equilibrium, a coordinate transformation from the intermediate to the reference configuration is necessary. In the three-dimensional Euclidean coordinate space, the coordinate system in intermediate configuration can be expressed in terms of the growth part of the deformation gradient and the coordinate system in the reference configuration. For the special case of isotropic volumetric growth, it can be reduced to a linear mapping using the volumetric stretch ratio ϑ which leads to the transformation factors ϑ^2 and

16177061, 0, Downloaded from https://onlinelibrary.wiley.com/doi/10.1002/pamm.202400200 by Rwth Aachen Hochschulbibliothek, Wiley Online Library on [11/09/2024]. See the Terms and Conditions (https://onlinelibrary.wiley.com/terms-and-conditions) on Wiley Online Library for rules of use; OA articles are governed by the applicable Creative Commons License

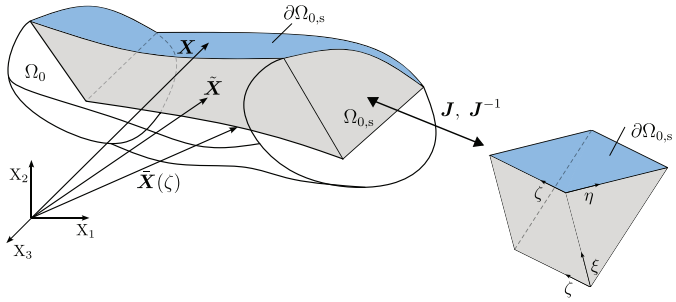


FIGURE 2 Three-dimensional solid domain Ω_0 in the physical space (left) of the undeformed configuration, with a highlighted section $\Omega_{0,s}$ in grey and its boundaries $\partial\Omega_{0,s}$ in blue. The section depicted in the parameter space (right) is spanned by the boundary coordinates η and ζ and the scaling parameter ξ. Figure after ref. [11].

ϑ^4 for tensor of second and fourth order, respectively

$$\hat{\mathbf{e}}_i = \mathbf{F}_g\,\mathbf{e}_i = \vartheta\,\mathbf{e}_i \quad \Rightarrow \quad \hat{\mathbf{S}} = \hat{S}_{ij}\,\mathbf{e}_i \otimes \mathbf{e}_j\,\vartheta^2 \quad \text{and} \quad \hat{\mathbb{C}}^{eg} = \hat{\mathbb{C}}^{eg}_{ijkl}\,\mathbf{e}_i \otimes \mathbf{e}_j \otimes \mathbf{e}_k \otimes \mathbf{e}_l\,\vartheta^4 \quad \Big| \quad i,j,k,l \in \{1,2,3\}. \tag{8}$$

2.2 | Generalized scaled boundary isogeometric analysis

The irregular and diverse geometries of naturally grown timber elements pose a significant challenge when it comes to describing their cross-sections and calculating them in a computational model. For example, effects from the main direction of growth, such as curvature or branching, must be considered in a static analysis [2]. With the help of 3D laser scanning techniques or photogrammetry, tree elements or entire trees can be mapped geometrically and used as the basis for construction elements [7]. The specific workpath from the physical specimen to the numerical model is shown in ref. [8]. The point cloud models created in this way generate the geometric center line and the enveloping lateral surface. Both are based on NURBS curves or NURBS surfaces; in this case, NURBS means non-uniform rational b-splines. By combining these with a scaled boundary method only a two-dimensional surface is needed to describe a three-dimensional body. Only the lateral faces and the center line are modeled. Figures 1 and 2 shows this concept and the underlying parametrization.

2.2.1 | Parametrization

The parametric description is based on the scaled boundary isogeometric analysis from refs. [9, 10] and was developed in ref. [11]. As highlighted in Figure 2, is the geometric body Ω_0 described by its lateral surface and a center line. The boundary surface and, with that, the body is subdivided into several sections $\Omega_{0,s}$. Each boundary section is spanned by the boundary parameters η (in the tangential direction) and ζ (in the longitudinal direction); the scaling parameter ξ is introduced for the spatial direction. An arbitrary point on the boundary can be expressed as

$$\tilde{\boldsymbol{X}}(\eta,\zeta) = \mathbf{N}_b(\eta,\,\zeta)\boldsymbol{X}_s \quad \text{on } \partial\Omega_{0,s}\,, \tag{9}$$

while an arbitrary point on the center line can be expressed as

$$\bar{\boldsymbol{X}}(\zeta) = \mathbf{N}_j(\zeta)\boldsymbol{X}_0\,. \tag{10}$$

Hereby contains the vector $\boldsymbol{X}_s$ all sectional coordinates of the control points on the boundary, while $\boldsymbol{X}_0$ contains all coordinates of the center line. The matrices $\mathbf{N}_b$ and $\mathbf{N}_j$ contain the approach functions of the boundary and the center line. The position vector of an arbitrary point $\boldsymbol{X}$ in the interior of the domain is described by the multiplication of the scaling parameter ξ with the difference between the boundary and the center line.

$$\begin{aligned}\boldsymbol{X}(\xi,\eta,\zeta) &= \xi\Big(\tilde{\boldsymbol{X}}(\eta,\zeta) - \bar{\boldsymbol{X}}(\zeta)\Big) + \bar{\boldsymbol{X}}(\zeta) \\ &= \xi\,\mathbf{N}_b(\eta,\zeta)\boldsymbol{X}_s + (1-\xi)\mathbf{N}_j(\zeta)\boldsymbol{X}_0 \qquad \text{in } \Omega_{0,s}\,.\end{aligned} \tag{11}$$

16177061, 0, Downloaded from https://onlinelibrary.wiley.com/doi/10.1002/pamm.202400200 by Rwth Aachen Hochschulbibliothek, Wiley Online Library on [11/09/2024]. See the Terms and Conditions (https://onlinelibrary.wiley.com/terms-and-conditions) on Wiley Online Library for rules of use; OA articles are governed by the applicable Creative Commons License

Since these relations are defined in the parametric domain, but a formulation for the physical space is needed, the partial derivatives need to be mapped from one in another. For this, the Jacobian matrix $\boldsymbol{J}$ is defined with

$$\boldsymbol{J}(\xi,\eta,\zeta)=\begin{bmatrix}\frac{\partial X_1}{\partial\xi} & \frac{\partial X_2}{\partial\xi} & \frac{\partial X_3}{\partial\xi}\\ \frac{\partial X_1}{\partial\eta} & \frac{\partial X_2}{\partial\eta} & \frac{\partial X_3}{\partial\eta}\\ \frac{\partial X_1}{\partial\zeta} & \frac{\partial X_2}{\partial\zeta} & \frac{\partial X_3}{\partial\zeta}\end{bmatrix}=\begin{bmatrix}1&0&0\\0&\xi&0\\0&0&1\end{bmatrix}\underbrace{\begin{bmatrix}\tilde{X}_1-\bar{X}_1 & \tilde{X}_2-\bar{X}_2 & \tilde{X}_3-\bar{X}_3\\ \frac{\partial\tilde{X}_1}{\partial\eta} & \frac{\partial\tilde{X}_2}{\partial\eta} & \frac{\partial\tilde{X}_3}{\partial\eta}\\ \frac{\partial X_1}{\partial\zeta} & \frac{\partial X_2}{\partial\zeta} & \frac{\partial X_3}{\partial\zeta}\end{bmatrix}}_{\bar{\boldsymbol{J}}}. \tag{12}$$

A formulation for the determinant of the Jacobian matrix is given by $\det\boldsymbol{J}=\xi\det\bar{\boldsymbol{J}}$, with

$$\bar{\boldsymbol{J}}(\xi,\eta,\zeta)=\begin{bmatrix}\tilde{X}_1-\bar{X}_1 & \tilde{X}_2-\bar{X}_2 & \tilde{X}_3-\bar{X}_3\\ \frac{\partial\tilde{X}_1}{\partial\eta} & \frac{\partial\tilde{X}_2}{\partial\eta} & \frac{\partial\tilde{X}_3}{\partial\eta}\\ \xi\frac{\partial\tilde{X}_1}{\partial\zeta}+(1-\xi)\frac{\partial\bar{X}_1}{\partial\zeta} & \xi\frac{\partial\tilde{X}_2}{\partial\zeta}+(1-\xi)\frac{\partial\bar{X}_2}{\partial\zeta} & \xi\frac{\partial\tilde{X}_3}{\partial\zeta}+(1-\xi)\frac{\partial\bar{X}_3}{\partial\zeta}\end{bmatrix}. \tag{13}$$

The volume increment is mapped from the parametric space into the physical space with $\mathrm{d}V=\xi\det\bar{\boldsymbol{J}}\,\mathrm{d}\xi\,\mathrm{d}\eta\,\mathrm{d}\zeta$. Furthermore, it holds

$$\begin{aligned}\det\bar{\boldsymbol{J}} &= (\tilde{X}_1-\bar{X}_1)\left(\frac{\partial\tilde{X}_2}{\partial\eta}\left(\xi\frac{\partial\tilde{X}_3}{\partial\zeta}+(1-\xi)\frac{\partial\bar{X}_3}{\partial\zeta}\right)-\frac{\partial\tilde{X}_3}{\partial\eta}\left(\xi\frac{\partial\tilde{X}_2}{\partial\zeta}+(1-\xi)\frac{\partial\bar{X}_2}{\partial\zeta}\right)\right)\\ &+(\tilde{X}_2-\bar{X}_2)\left(\frac{\partial\tilde{X}_3}{\partial\eta}\left(\xi\frac{\partial\tilde{X}_1}{\partial\zeta}+(1-\xi)\frac{\partial\bar{X}_1}{\partial\zeta}\right)-\frac{\partial\tilde{X}_1}{\partial\eta}\left(\xi\frac{\partial\tilde{X}_3}{\partial\zeta}+(1-\xi)\frac{\partial\bar{X}_3}{\partial\zeta}\right)\right)\\ &+(\tilde{X}_3-\bar{X}_3)\left(\frac{\partial\tilde{X}_1}{\partial\eta}\left(\xi\frac{\partial\tilde{X}_2}{\partial\zeta}+(1-\xi)\frac{\partial\bar{X}_2}{\partial\zeta}\right)-\frac{\partial\tilde{X}_2}{\partial\eta}\left(\xi\frac{\partial\tilde{X}_1}{\partial\zeta}+(1-\xi)\frac{\partial\bar{X}_1}{\partial\zeta}\right)\right).\end{aligned} \tag{14}$$

The differential operator in matrix notation is expressed by

$$\mathbf{D}=\begin{bmatrix}\frac{\partial}{\partial X_1}&0&0&\frac{\partial}{\partial X_2}&0&\frac{\partial}{\partial X_3}&0&0&0\\ 0&\frac{\partial}{\partial X_2}&0&0&\frac{\partial}{\partial X_1}&0&0&\frac{\partial}{\partial X_3}&0\\ 0&0&\frac{\partial}{\partial X_3}&0&0&0&\frac{\partial}{\partial X_1}&0&\frac{\partial}{\partial X_2}\end{bmatrix}^{\mathrm{T}}. \tag{15}$$

2.2.2 | Numerical approximation

The main concept of the isogeometric analysis, as initially demonstrated by ref. [12], is to use the geometry functions (NURBS) as used in computer-aided design (CAD) programs not solely for the exact description of the geometry but directly for the determination of the solution field. The use of NURBS has a big advantage in modeling freeform shapes and benefits of the vast amount of efficient algorithms for refinement and the higher $C^{\mathrm{p}-1}$-continuity for p-th order NURBS in comparison to the finite element analysis (FEA). Consequently, the displacements on the sectional boundary surface $\tilde{\boldsymbol{u}}$ are approximated with the same functions that describe the geometry.

$$\begin{aligned}\boldsymbol{u}&=\sum_{\mathrm{I}=1}^{\mathrm{n_{bc}}}R_{\mathrm{I}}^{\mathrm{p,q}}\boldsymbol{u}_{\mathrm{s,I}}=\mathbf{N}_{\mathrm{b}}(\eta,\zeta)\boldsymbol{u}_{\mathrm{s}}(\xi)\\ &=\begin{bmatrix}R_1^{\mathrm{p,q}}&0&0&&R_{\mathrm{n_{bc}}}^{\mathrm{p,q}}&0&\\ 0&R_1^{\mathrm{p,q}}&0&\dots&0&R_{\mathrm{n_{bc}}}^{\mathrm{p,q}}&0\\ 0&0&R_1^{\mathrm{p,q}}&&0&0&R_{\mathrm{n_{bc}}}^{\mathrm{p,q}}\end{bmatrix}\begin{bmatrix}\boldsymbol{u}_1\\ \boldsymbol{u}_2\\ \boldsymbol{u}_3\\ \vdots\\ \boldsymbol{u}_{\mathrm{s,n_{bc}}}\end{bmatrix}.\end{aligned} \tag{16}$$

16177061, 0, Downloaded from https://onlinelibrary.wiley.com/doi/10.1002/pamm.202400200 by Rwth Aachen Hochschulbibliothek, Wiley Online Library on [11/09/2024]. See the Terms and Conditions (https://onlinelibrary.wiley.com/terms-and-conditions) on Wiley Online Library for rules of use; OA articles are governed by the applicable Creative Commons License

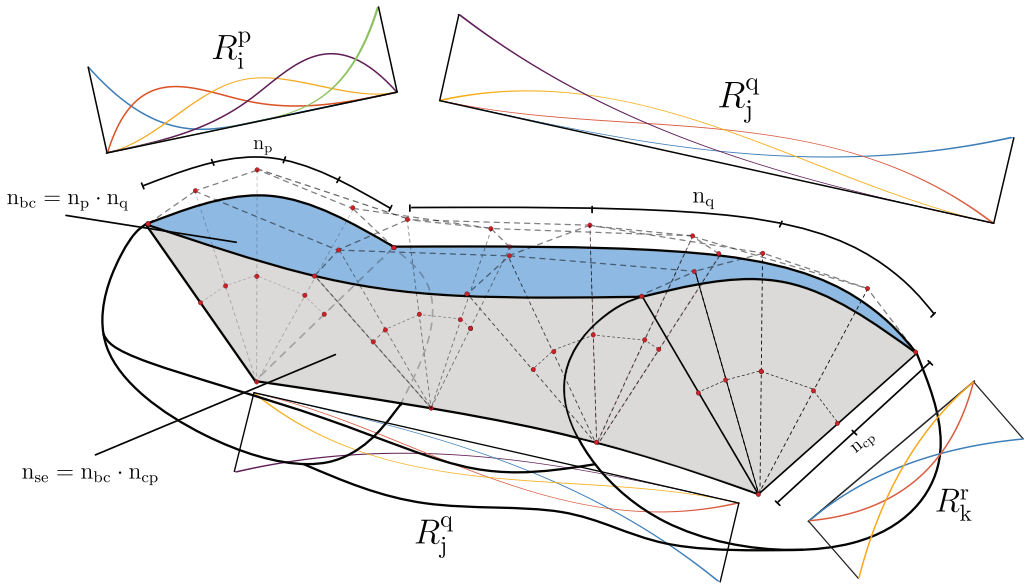


FIGURE 3 Modified scaled boundary section in physical space with NURBS basis functions in η, ζ direction. Basis functions $R_i^p(\eta)$ and $R_j^q(\zeta)$ on the boundary and $R_j^q(\zeta)$ in longitudinal direction on the center line. Additional basis function plotted $R_k^r(\xi)$ in scaling direction. Number of control points of a single section on boundary surface n_{bc}, on each individual scaling line n_{cp} and in the total domain n_{se}.

Here, $\boldsymbol{u}_{s,I}$ contains the displacements of the I-th control point of the n_{bc} control points on the sectional boundary surfaces. The individual basis function, its affiliation and the number of particular control points are depicted in Figure 3, separated in the three independent parametric directions. The corresponding surface NURBS function of the orders p and q is described by $R_I^{p,q}$. The displacement vector $\boldsymbol{u}_{r,I}$ is associated with the n_{cp} control points on each individual scaling line in the spatial direction.

$$\begin{aligned}\boldsymbol{u}_{s,I}(\xi) &= \sum_{k=1}^{n_{cp}} R_k^r(\xi)\boldsymbol{u}_k = \mathbf{N}_{s,I}(\xi)\boldsymbol{u}_{r,I} \\ &= \begin{bmatrix} R_1^r & 0 & 0 & & R_{n_{cp}}^r & 0 & \\ 0 & R_1^r & 0 & \dots & 0 & R_{n_{cp}}^r & 0 \\ 0 & 0 & R_1^r & & 0 & 0 & R_{n_{cp}}^r \end{bmatrix} \begin{bmatrix} \boldsymbol{u}_1 \\ \boldsymbol{u}_2 \\ \boldsymbol{u}_3 \\ \vdots \\ \boldsymbol{u}_{n_{cp}} \end{bmatrix}\end{aligned} \tag{17}$$

The k-th NURBS-function of order r in scaling direction is denoted by R_k^r.

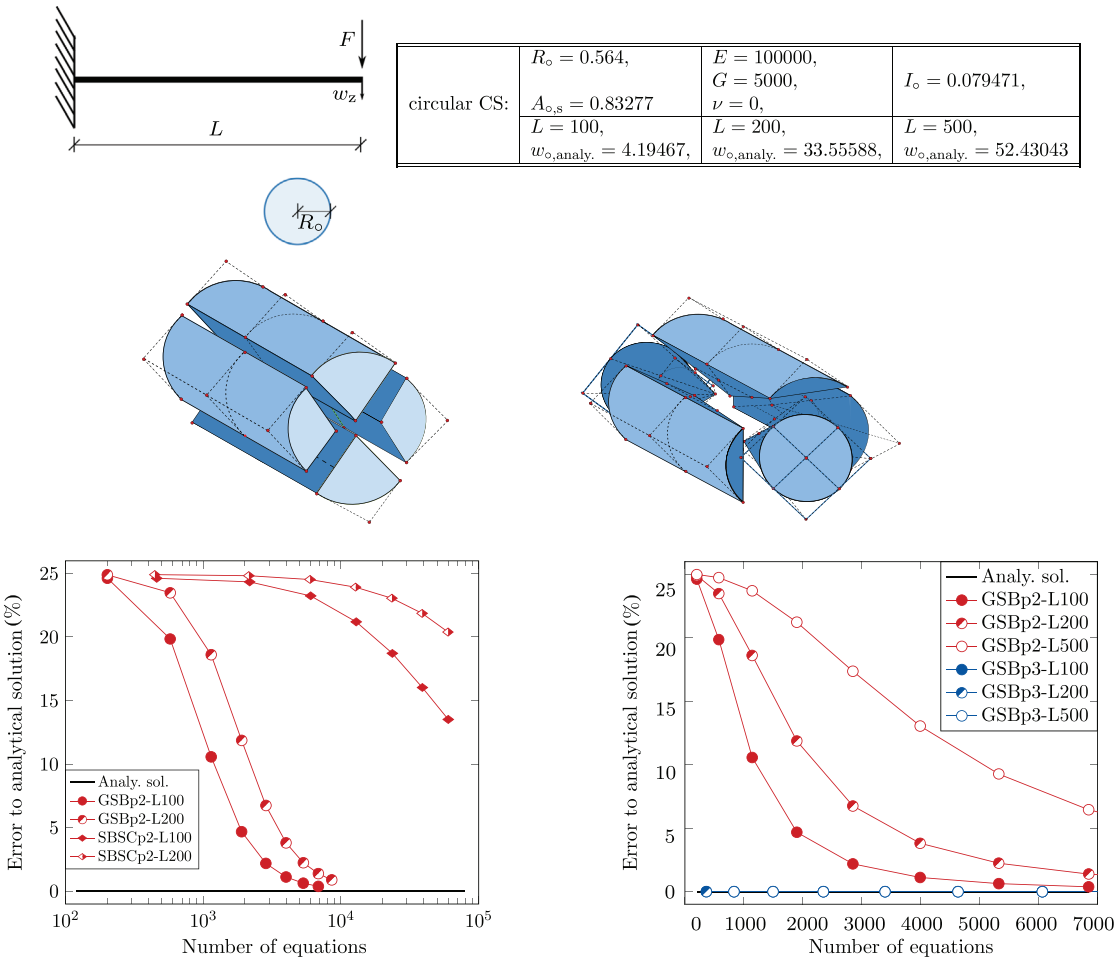
$$\boldsymbol{u}(\xi,\eta,\zeta) = \mathbf{N}_b\mathbf{N}_s\boldsymbol{U} \quad . \tag{18}$$

The vector $\boldsymbol{U}$ contains all of the $3 \cdot n_{se} = 3 \cdot n_{bc} \cdot n_{cp}$ nodal degrees of freedom in the scaling direction.

3 | NUMERICAL EXAMPLES

This chapter evaluates the GSBIGA element formulation on suitable numerical examples and tests the implemented growth material routine on reference examples and possible applications. The numerical calculations were realized in the chair's extended version of the FEA program (FEAP) [13]. The units in all examples are omitted but are chosen to be consistent.

16177061, 0, Downloaded from https://onlinelibrary.wiley.com/doi/10.1002/pamm.202400200 by Rwth Aachen Hochschulbibliothek, Wiley Online Library on [11/09/2024]. See the Terms and Conditions (https://onlinelibrary.wiley.com/terms-and-conditions) on Wiley Online Library for rules of use; OA articles are governed by the applicable Creative Commons License



circular CS:	$R_\circ = 0.564$,	$E = 100000$,	
	$A_{\circ,s} = 0.83277$	$G = 5000$,	$I_\circ = 0.079471$,
		$\nu = 0$,	
	$L = 100$,	$L = 200$,	$L = 500$,
	$w_{\circ,\text{analy.}} = 4.19467$,	$w_{\circ,\text{analy.}} = 33.55588$,	$w_{\circ,\text{analy.}} = 52.43043$

FIGURE 4 Comparison between GSBIGA (GSB), conventional SBIGA (SBSC) and reference solution for a cantilever bending test in *z*-direction for varying length L on the left. Number of elements per surface direction is varied between $n = 2$ and 16. Comparison between different orders of NURBS functions p and q for GSBIGA on the right [11]. GSBIGA, generalized scaled boundary isogeometric analysis.

3.1 | Cantilever test

The first numerical example comprises a bending test in the *z*-direction on a cantilever beam with a circular cross-section. The schematic structure, the material properties, and results are depicted in Figure 4. During the test, the cantilever's slenderness varied between L = 100 and 500 for a constant cross-section area. A sketch of the patches is plotted in the middle. The GSBIGA patches are uniformly shaped triangular prisms; here, only the lateral surface is modeled. The conventional SBIGA model is divided into six patches. The patches get distorted, especially for a higher slenderness. In the plots, the number of control points and elements is varied. The plots indicate that the relative error of GSBIGA compared to the analytical solution is lower than the relative error of SBIGA compared to the analytical solution. It is evident that the GSBIGA is much more stable against numerical errors due to long, flat elements. There is still a residual length dependence for the quadratic GSBIGA. In the cubic case, the GSBIGA directly converges to the analytical solution. This is without a sophisticated locking formulation and simple displacement volume elements. Further information is given in ref. [11].

3.2 | Bifurcation test

When modeling bifurcated structural elements, several surface sections and center lines are required in the longitudinal direction. Branch forks are divided into several surface sections. The various NURBS surfaces and the center lines must be flush at the connecting boundaries. The subdivision occurs at the fork point, whereby the different areas are rigidly

16177061, 0, Downloaded from https://onlinelibrary.wiley.com/doi/10.1002/pamm.202400200 by Rwth Aachen Hochschulbibliothek, Wiley Online Library on [11/09/2024]. See the Terms and Conditions (https://onlinelibrary.wiley.com/terms-and-conditions) on Wiley Online Library for rules of use; OA articles are governed by the applicable Creative Commons License

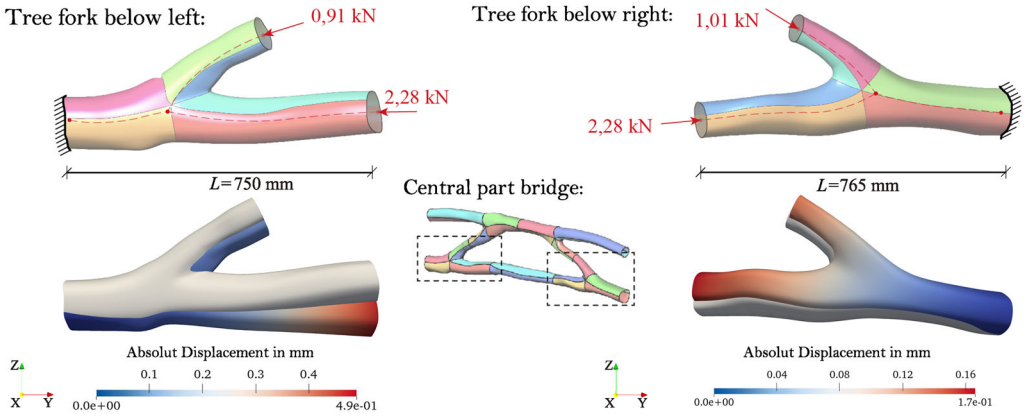


FIGURE 5 Calculation of bifurcated parts of bridge build in university project at Chair of Structures and Structural Design, RWTH Aachen University. External loads are taken from the auxiliary structural bar model. The displacement field on the deformed model is plotted below.

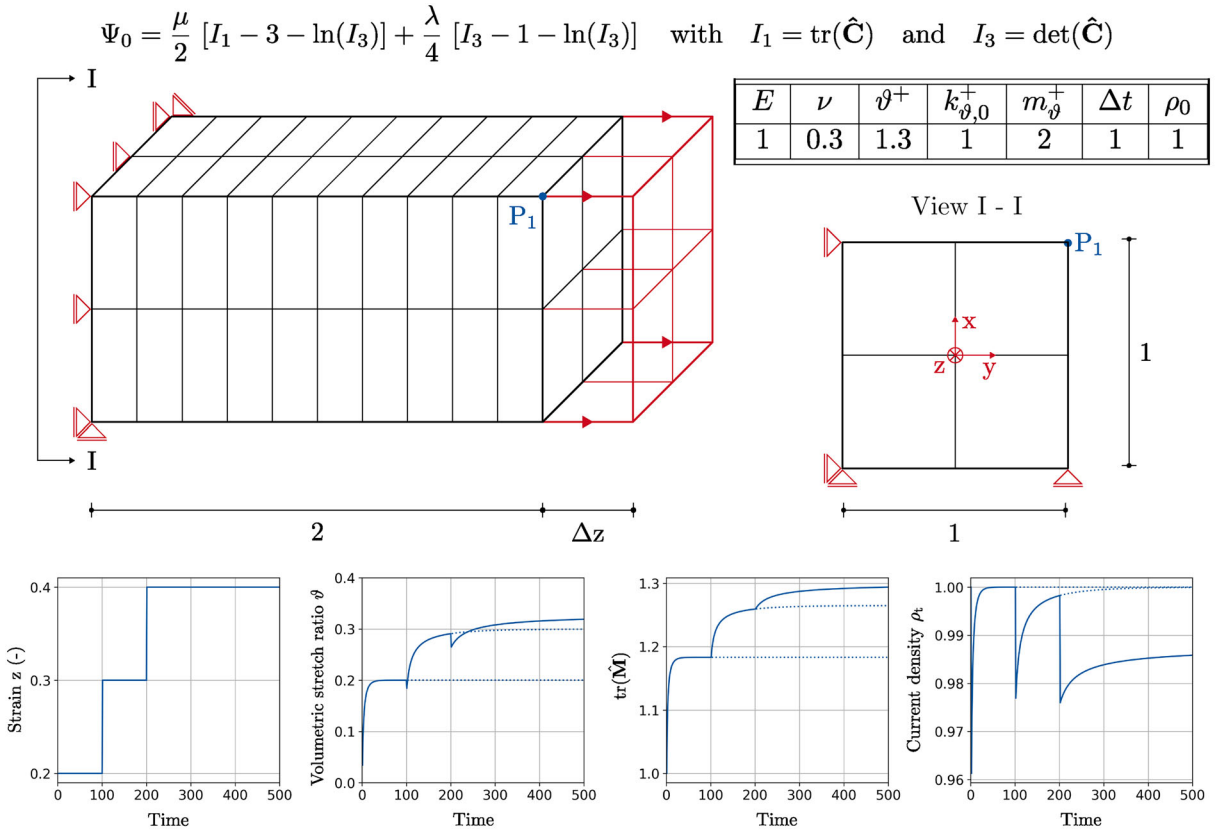


FIGURE 6 3D cantilever undergoing uniaxial stretch, its boundaries, cross-section and coordinate axes. Strains in longitudinal z-axis, the volumetric stretch ratio ϑ, the trace of the Mandel stress $\mathrm{tr}(\hat{\mathbf{M}})$ and the current density ρ_t in the c.c. at the point P_1 plotted below.

connected. Figure 5 shows two branch forks from the bridge model, including the boundary conditions and the applied load. The structure is loaded in the direction of the longitudinal axes and restrained at the supports. The forces correspond to the normal forces from the simplified beam model. In the bottom row of Figure 5 the deformed geometries are plotted over the undeformed structure. The displacement field is plotted on the deformed body and resolves in the expected deformations.

16177061, 0, Downloaded from https://onlinelibrary.wiley.com/doi/10.1002/pamm.202400200 by Rwth Aachen Hochschulbibliothek, Wiley Online Library on [11/09/2024]. See the Terms and Conditions (https://onlinelibrary.wiley.com/terms-and-conditions) on Wiley Online Library for rules of use; OA articles are governed by the applicable Creative Commons License

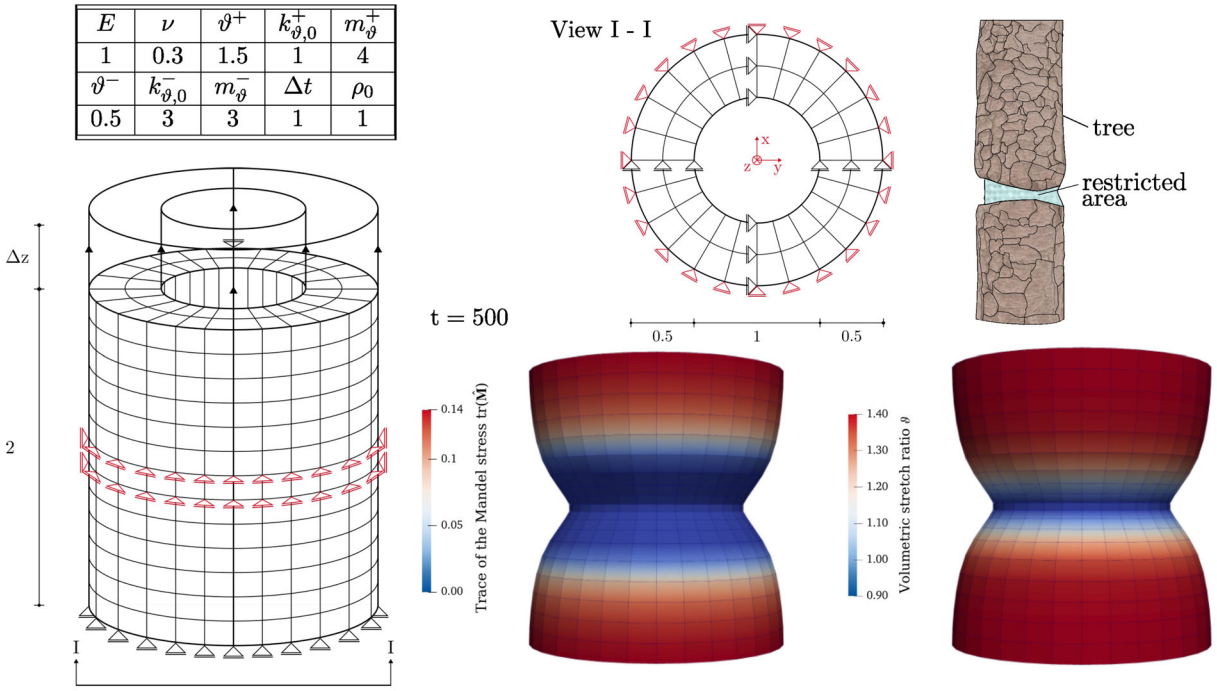


FIGURE 7 Modeling of restricted tree like growth through external boundaries undergoing uniaxial stretch. Applied load of 50% stretch and plots at t = 500.

3.3 | Uniaxial stretch test

For the following growth examples, a Neo-Hooke type material combined with standard geometrical linear 3D-solid elements was used. The potential Ψ_0 per unit volume of the Neo-Hooke type material is given in Figure 6. The first example of volumetric isotropic growth corresponds to the uniaxial tensile test. As can be seen, the load is uniaxial and displacement-driven. The load is applied in three individual steps (20%, 30%, and 40% elongation). As the volumetric stretch ratio plot shows, the growth process is initially faster and then slowly approaches its final state, the so-called biological equilibrium. At this equilibrium, the stresses, including the Mandel stress, return to zero. This only applies as long as the growth capacity (in this case ϑ^+) has not yet been reached. The last load step to 40% elongation exceeds the growth capacity of the material, and the elongation ratio ϑ converges to its limit value ϑ^+. Now the current density ρ_t converges to a value that is smaller than the original density ρ_0, as the internal mass source cannot compensate for the applied strain. Residual elastic stresses occur.

3.4 | Restricted growth

As a last example, the growth model was applied to the timber realm of influenced growth by external boundaries. The geometric and material description and the results at t = 500 are shown in Figure 7. At this point, the stretch capacity has not yet been reached, so rest stresses remain. The Mandel stress will vanish at the time of convergence; only in the vicinity of the restricted area will non-zero stresses remain.

4 | CONCLUSION

Since standard engineering calculations simplify grown timber cross-sections, GSBIGA was presented as a numerical method for calculating long and slender objects. An automated process from naturally shaped timber to simulation was developed based on 3D-scanned surface data. An accurate representation of the original geometry is essential, as even small deflections or eccentricities can majorly impact stresses and deformations. In the future, the focus will be on extend-

16177061, 0, Downloaded from https://onlinelibrary.wiley.com/doi/10.1002/pamm.202400200 by Rwth Aachen Hochschulbibliothek, Wiley Online Library on [11/09/2024]. See the Terms and Conditions (https://onlinelibrary.wiley.com/terms-and-conditions) on Wiley Online Library for rules of use; OA articles are governed by the applicable Creative Commons License

ing the isotropic, linear elastic material model to a more realistic material model that can be used to model the anisotropic material properties of wood. As the spanning element coordinate axes of the numerical model correspond to the polar preferred directions of the material wood, the two are closely coupled. The natural strength of GSBIGA is its efficient description of slender and curved structures. In addition, it combines the advantages of isogeometric analysis with those of scaled surfaces and provides a parametric description that matches the wood structure. Thus, realistic applications of a volumetric growth material in the timber field were modeled. In the future, the focus will be on extending this to an anisotropic growth model and coupling it with the GSBIGA.

ACKNOWLEDGMENTS

The financial support of the Deutsche Forschungsgemeinschaft (DFG, German Research Foundation) under Grant No. KL 1345/18-1 (Project No. 512769030) is gratefully acknowledged.

Open access funding enabled and organized by Projekt DEAL.

ORCID

Florian Spahn https://orcid.org/0009-0007-3903-7571
Florian Kolisch https://orcid.org/0009-0002-0105-1494
Maximilian Praster https://orcid.org/0000-0002-6346-0253
Elizabeth Rosado Balmayor https://orcid.org/0000-0002-0484-4847
Sven Klinkel https://orcid.org/0000-0003-1535-0823

REFERENCES

1. Riedel, T., Hennig, P., Kroiher, F., Polley, H., Schmitz, F., & Schwitzgebel, F. (2017). *Die dritte Bundeswaldinventur (BWI 2012)*. Inventur- und Auswertemethoden.
2. Moreno Gata, K., Musto, J., & Trautz, M. (2020). *eCAADe proceedings*, *eCAADe 2020*, 51–59.
3. Ludwig, F., Schwertfeger, H., & Storz, O. (2012). Living systems designing growth in baubotanik. *Architectural Design*, *82*(2), 82–87.
4. Wang, X., Gard, W., Borska, H., Ursem, B., & van de Kuilen, J. W. G. (2020). Vertical greenery systems: From plants to trees with self-growing interconnections. *European Journal of Wood and Wood Products*, *78*, 1031–1043.
5. Graefe, R. (2014). *Arbeitsblätter zur Baugeschichte*. Geymüller | Verl. für Architektur.
6. Himpel, G., Kuhl, E., Menzel, A., & Steinmann, P. (2005). Computational modelling of isotropic multiplicative growth. *Computer Modeling in Engineering & Sciences*, *8*, 119–134.
7. Moreno Gata, K., Seiter, A., Grizmann, D., & Trautz, M. (2023). Development of construction methods with naturally grown timber and bending-resistant joints. *WCTE Proceedings, WCTE 2023*, 705–710.
8. Spahn, F., Moreno Gata, K., Trautz, M., & Klinkel, S. (2024). Application of raw wood elements for load-bearing structures and mechanical analysis using image-based simulation methods. *Bauingenieur*, *99*(4), 109–116.
9. Chen, L., Simeon, B., & Klinkel, S. (2016). A NURBS based Galerkin approach for the analysis of solids in boundary representation. *Computer Methods in Applied Mechanics and Engineering*, *305*, 777–805.
10. Chasapi, M., Mester, L., Simeon, B., & Klinkel, S. (2021). Isogeometric analysis of 3D solids in boundary representation for problems in nonlinear solid mechanics and structural dynamics. *International Journal for Numerical Methods in Engineering*, *123*(5), 1228–1252.
11. Spahn, F., Moreno Gata, K., Trautz, M., & Klinkel, S. (2024). Generalised scaled boundary isogeometric analysis - a method for structural analysis of naturally shaped timber structures. *Wood Material Science and Engineering*. https://doi.org/10.1080/17480272.2024.2323590
12. Hughes, T., Cottrell, J. A., & Bazilevs, Y. (2005). Isogeometric analysis: CAD, finite elements, NURBS, exact geometry and mesh refinement. *Computer Methods in Applied Mechanics and Engineering*, *194*(39–41), 4135–4195.
13. Taylor, R. L. (2014). *FEAP - Finite Element Analysis Program*. University of California.

How to cite this article: Spahn, F., Kolisch, F., Praster, M., Balmayor, E. R., & Klinkel, S. (2024). Isotropic growth model for generalized scaled boundary isogeometric analysis on slender structures. *Proceedings in Applied Mathematics and Mechanics*, e202400200. https://doi.org/10.1002/pamm.202400200

16177061, 0, Downloaded from https://onlinelibrary.wiley.com/doi/10.1002/pamm.202400200 by Rwth Aachen Hochschulbibliothek, Wiley Online Library on [11/09/2024]. See the Terms and Conditions (https://onlinelibrary.wiley.com/terms-and-conditions) on Wiley Online Library for rules of use; OA articles are governed by the applicable Creative Commons License